

# The nearest neighbor statistics for X-ray source counts

## I. The method

A. M. Sołtan

Nicolaus Copernicus Astronomical Center, Bartycka 18, 00-716 Warsaw, Poland  
e-mail: soltan@camk.edu.pl

Received / Accepted

### ABSTRACT

**Context.** Most of the X-ray background (XRB) is generated by discrete X-ray sources. It is likely that still unresolved fraction of the XRB is composed from a population of the weak sources below the present detection thresholds and a truly diffuse component. It is a matter of discussion a nature of these weak sources.

**Aims.** The goal is to explore the effectiveness of the nearest neighbor statistics (NNST) of the photon distribution for the investigation of the number counts of the very weak sources.

**Methods.** All the sources generating at least two counts each induce a nonrandom distribution of counts. This distribution is analyzed by means of the NNST. Using the basic probability equations, the relationships between the source number counts  $N(S)$  and the NNST are derived.

**Results.** It is shown that the method yields constraints on the  $N(S)$  relationship below the regular discrete source detection threshold. The NNST was applied to the medium deep *Chandra* pointing to assess the source counts  $N(S)$  at flux levels attainable only with the very deep exposures. The results are in good agreement with the direct source counts based in the *Chandra* Deep Fields (CDF).

**Conclusions.** In the next paper of this series the NNST will be applied to the the CDF to assess the source counts below the present flux limits.

**Key words.** X-rays: diffuse background – X-rays: general

## 1. Introduction

The X-ray background (XRB) is mostly generated by discrete extragalactic sources (e.g. Lehmann et al. 2001; Kim et al. 2007, and references therein). Thus, the source counts provide the essential information on the constituents of the XRB and the X-ray  $N(S)$  relationship has been a subject of numerous studies for the last 40 years.

The individual point-like source is detected if a number of counts within a specified area exceeds the assumed threshold. Size of the detection box is defined by the Point Spread Function (PSF), while the detection threshold is usually selected to minimize number of false detections and at the same time to maximize number of the real sources. The detection threshold is typically set at the level of  $4 - 5\sigma$  above the local average count density. A presence of weaker sources, below the formal detection threshold, is manifested by the increased fluctuations of the count distribution as compared to the fluctuations expected for the random counts.

A common approach to assess counts of sources weaker than the detection limit is based on the count density fluctuation analysis. To quantify signal generated by the discrete sources one should determine the intensity distribution  $P(D)$ , i.e. the histogram of the number of pixels as a function of the number of counts. The observed function  $P(D)$  is then compared with the functions obtained from the simulated count distributions (e.g. Hasinger et al., 1993; Miyaji & Griffiths, 2002). It is assumed that the simulated source counts represent the actual source distribution if the model  $P(D)$  function mimics the observed his-

toqram. A contribution of point sources to the count distribution one can estimate also using the auto-correlation function (ACF). Since the integral of the ACF is directly related to the second moment of the  $P(D)$  distribution, (e.g. Sołtan, 1991) both methods are closely related.

An innovative method to assess the number of weak sources was proposed by Georgakakis et al. (2008). In their approach the count distribution in the detection cell is explicitly expressed as a sum of the source and background counts. As a result of a rigorous application of the Poisson statistics, a flux probability distribution is derived as a function of the total and background counts observed in the detection cell. This probability distribution combined with the adequately defined sensitivity map of a given observation is then used to estimate the the source number counts.

The count fluctuations are proportional to the source intensities. Thus, the observed fluctuation amplitude is dominated by the sources just below the detection threshold set for the individual objects, whereas it is only weakly sensitive to the fainter sources which produce smaller number of counts. One should note, however, that every source which produces more than one count generates deviation from the random count distribution. In the present paper we investigate the efficiency of the nearest neighbor statistics (NNST) for the weak source analysis and we show that the NNST is a powerful tool to estimate the source counts,  $N(S)$ , down to very low flux levels. We apply this technique to one of the *Chandra* AEGIS fields with the exposure of 465 ks. The NNST allows us to obtain the  $N(S)$  relationship extending down to  $2 \times 10^{-17}$  erg cm<sup>-2</sup>s<sup>-1</sup> and  $7 \times 10^{-17}$  erg cm<sup>-2</sup>s<sup>-1</sup> in the 0.5 – 2 keV and 2 – 8 keV energy bands, respectively, i.e. a factor of 5 – 10 below the stan-

standard sensitivity threshold corresponding to this exposure. Since the present count estimates are contained within the flux range covered by the direct source counts derived from the deepest *Chandra* fields (such as CDFS), the effectiveness of the NNST method could be directly assessed.

The organization of the paper is as follows. In the next section, the method and all the relevant formulae are presented. Then, in Sect. 3, the observational material is described and the computational details including questions related to the PSF are given. Results of the calculations, i.e. estimates of the source counts below the nominal sensitivity limit are presented in Sect. 4. The results are summarized and discussed in Sect. 5. Prospects for the application of the NNST to the deep *Chandra* fields are presented.

## 2. The nearest neighbor statistics

In this section a general formulae based on the theory of probability are derived, while all the details related to the actual observations (e.g. relationship between counts and photon energy, instrument sensitivity) are discussed in Sect. 3.

In the present consideration we assume that counts in the given *Chandra* ACIS<sup>1</sup> observation are distributed according to the following model: some a priori unknown fraction of counts is randomly distributed, i.e. the positions of the counts are fully described by the Poisson statistics, while all the remaining photons are clustered in the point-like sources. Such model corresponds to the observation obtained using the idealized telescope without vignetting and detector with perfectly uniform response over the field of view. The real telescope-detector combination introduces numerous deformations to this ideal picture. We address this question below.

We further assume, that the positions of sources are also randomly distributed. Smoothly distributed counts constitute physically heterogeneous collection which contains both the particle background and various components of the foreground X-ray emission including scattered solar X-rays, the geocoronal oxygen lines as well as the thermal emission of hot plasma within our Galaxy (e.g. Hasinger, 1992; Galeazzi et al., 2007; Henley et al., 2007) and the emission by the WHIM (e.g. Soltan, 2007). Truly diffuse extragalactic background (Soltan, 2003) and weak discrete sources, each producing in the final image exactly one photon, contribute also to these counts. A separation of the extragalactic component from all the counts can be achieved in statistical terms using spectral information, however, individual event cannot be definitely classified as local or extragalactic.

Discrete sources in the deep X-ray exposures are predominantly extragalactic. Nevertheless, galactic sources are potentially present in the data and are included in the calculations. Photons coming from a discrete sources are distributed in the image in clumps defined by the PSF of the telescope.

Within the present model, statistical characteristics of the count distribution are fully defined: there are two population of events, the first is randomly distributed and the second is concentrated in the PSF shaped clusters. This feature of the count distribution is conveniently formulated using the NNST. Let  $n_t$  denotes the total number of counts in the investigated field,  $n_1$  - the number of events distributed randomly, or “single photons”,  $n_2$  - the number of photons due to sources producing each exactly 2 photons,  $n_3$  - number of photons due to “three photon” sources and so on. Thus,

$$n_1 + n_2 + \dots + n_k + \dots + n_{k_{\max}} = n_t, \quad (1)$$

<sup>1</sup> In all the analysis we use ACIS-I chips 0-3.

where the left hand side sum extends over all the sources and  $k_{\max}$  is the number photons produced by the brightest source in the field. The number of photons  $n_k$  is related to the number of sources in an obvious way:  $k N(k) = n_k$ , where  $N(k)$  denotes the number of “ $k$ -photon sources”.

Using the basic relationships of the probability theory, one can calculate  $P(r)$  – the probability that the distance to the nearest neighbor of a randomly chosen event exceeds  $r$ :

$$p_1 P(r|1) + p_2 P(r|2) + \dots + p_{k_{\max}} P(r|k_{\max}) = P(r), \quad (2)$$

where  $p_k$  denotes the probability that the randomly chosen photon is produced by the “ $k$ -photon source” ( $k = 1, 2, \dots, k_{\max}$ ), and  $P(r|k)$  is the conditional probability that there are no other counts within  $r$  provided the selected event belongs to the  $k$ -photon source.

The probability  $P(r)$  can be estimated for the given distribution of counts by measuring the distance to the nearest neighbor for the each photon in the field. Similarly,  $P(r|1)$  is given by the distribution of distances to the nearest photon from the randomly distributed points. Assuming that the distribution of “single counts” is not correlated with the distribution of photons from  $k \geq 2$  sources, and that sources are distributed randomly, the probability  $P(r|k)$  for  $k \geq 2$  are related to  $P(r|1)$  and to the PSF by the expression:

$$P(r|k) = P(r|1) \cdot \mathcal{P}(r|k), \quad (3)$$

where  $\mathcal{P}(r|k)$  is the probability that the distance from the randomly chosen photon produced by the  $k$ -photon source to its nearest neighbor from the same source exceeds  $r$ . This quantity is fully defined by the PSF.

To estimate the probabilities  $p_k$  we now use a ratio  $n_k/n_t$  and the Eq. 2 takes the form:

$$\frac{n_1}{n_t} P(r|1) + \sum_{k=2}^{k_{\max}} \frac{n_k}{n_t} P(r|1) \mathcal{P}(r|k) = P(r). \quad (4)$$

It is worth to note that Eq. 4 is linear in the photon counts  $n_k$ , what makes it particularly suitable for the estimates of the contribution of weak sources to the total counts. Both the second moment of the count distribution in pixels and the autocorrelation function depend on squares of the photon counts. Substituting successive values of  $r$  into Eq. 4, a set of linear equations is constructed which allows us to estimate the unknown counts  $n_k$ .

In the deep *Chandra* observation a large number of relatively strong sources is detected and the range of source fluxes is much too wide to apply Eq. 4 in the form given above where the source fluxes are listed consecutively from  $k = 2$  up to some maximum value of  $k_{\max}$  representing the strongest source in the field. Since we are interested in the counts at the faint end (down to  $k = 2$ ), the value of  $k_{\max}$  is selected at the conventional detection limit. All the sources above this threshold are pinpointed and removed from the data and the subsequent analysis is concentrated on the sources which cannot be individually recognized.

One can express the number of photons due to  $k$ -photon sources by means of the differential source counts  $N(S)$ :

$$n_k = k \int_{S_{\min}}^{S_{\max}} dS N(S) \mathfrak{P}(k|S), \quad (5)$$

where  $\mathfrak{P}(k|S)$  is the probability, that the source generating flux  $S$  delivers  $k$ -photons, while the integration limits  $S_{\min}$  and  $S_{\max}$

define the full range of the source fluxes. It is convenient to introduce the instrumental count as a flux unit. The flux  $s$  expressed in the ACIS counts in the definite observation is related to the flux in physical units,  $S$ , by:

$$s = S/cf, \quad (6)$$

where  $cf$  is the conversion factor which has units of “erg cm<sup>-2</sup> s<sup>-1</sup>/count” and is related to the parameter “exposure map” defined in a standard processing of the ACIS data<sup>2</sup>: exposure map =  $cf \cdot \langle E \rangle$ , where  $\langle E \rangle$  denotes the average photon energy.

For the power law source counts,  $N(s) = N_o s^{-b}$ , we have:

$$n_k = N_o \frac{\Gamma(k-b+1, s_{\min}) - \Gamma(k-b+1, s_{\max})}{\Gamma(k)}. \quad (7)$$

If the slope of the counts  $b$  is constant over a sufficiently wide range of fluxes (i.e.  $s_{\min} \ll 2$  and  $s_{\max} > k_{\max}$ ), one might replace the integration limits  $s_{\min}$  and  $s_{\max}$  by 0 and  $\infty$ , respectively, to get:

$$n_k = N_o \frac{\Gamma(k-b+1)}{\Gamma(k)}. \quad (8)$$

Thus, for the source counts represented by a single power law over sufficiently wide range of fluxes, Eq. 4 takes the form:

$$\frac{n_1}{n_t} P(r|1) + \frac{N_o}{n_t} \sum_{k=2}^{k_{\max}} \frac{\Gamma(k-b+1)}{\Gamma(k)} P(r|1) \mathcal{P}(r|k) = P(r). \quad (9)$$

The extension of this expression for the source counts with varying slope is straightforward. In particular, for the broken power law, the function  $\Gamma(k-b+1)$  is replaced by a proper combination of the incomplete gamma functions. Substituting

$$n_1 = n_t - \sum_{k=2}^{k_{\max}} n_k \quad (10)$$

and using Eq. 8 we finally get:

$$\frac{N_o}{n_t} P(r|1) \sum_{k=2}^{k_{\max}} \frac{\Gamma(k-b+1)}{\Gamma(k)} [1 - \mathcal{P}(r|k)] = P(r|1) - P(r). \quad (11)$$

Equation 11 contains two parameters which fully describe the power law source counts in the investigated flux range, viz. the normalization  $N_o$  and the slope  $b$ . Since the normalization at the flux  $s = k_{\max}$  is defined by the actual source counts above this threshold, only the slope remains unknown.

### 3. Observational material

To test efficiency of the present method I have selected a set of 16 close *Chandra* pointings within the AEGIS<sup>3</sup>. The observations span a period of 6 months and the data have been processed in a uniform way with the recent pipeline processing versions. The details of 16 observations used in the present paper are given in Table 1. All the exposures have been scrutinized with respect to the background flares and only “good time intervals” were used in the subsequent analysis. The data have been split into two energy bands: S – soft (0.5 – 2 keV) and H – hard (2 – 8 keV).

<sup>2</sup> See <http://asc.harvard.edu/ciao>. For the real observations, both the  $cf$  and exposure map are functions of the position. At this stage these parameters are assumed constant.

<sup>3</sup> All-wavelength Extended Groth strip International Survey, see <http://aegis.ucolick.org/index.html>.

**Table 1.** The *Chandra* AEGIS observations used in the paper

Obs. ID	Observation and processing dates		Processing version	Exposure time [s]
9450	2007-12-11	2007-12-13	7.6.11.3	29100
9451	2007-12-16	2008-01-02	7.6.11.4	25350
9793	2007-12-19	2007-12-21	7.6.11.4	44750
9725	2008-03-31	2008-04-02	7.6.11.6	28050
9842	2008-04-02	2008-04-03	7.6.11.6	19450
9844	2008-04-05	2008-04-06	7.6.11.6	34600
9866	2008-06-03	2008-06-05	7.6.11.6	31450
9726	2008-06-05	2008-06-06	7.6.11.6	39750
9863	2008-06-07	2008-06-07	7.6.11.6	24100
9873	2008-06-11	2008-06-12	7.6.11.6	30850
9722	2008-06-13	2008-06-15	7.6.11.6	19900
9453	2008-06-15	2008-06-17	7.6.11.6	22150
9720	2008-06-17	2008-06-18	7.6.11.6	26000
9723	2008-06-18	2008-06-20	7.6.11.6	30950
9876	2008-06-22	2008-06-23	7.6.11.6	25050
9875	2008-06-23	2008-06-25	7.6.11.6	33150
Total exposure				464650

#### 3.1. The exposure map

The observations, listed in Table 1 were merged to create a single count distribution and exposure map. A circular area covered by all the pointings with a relatively uniform exposure, centered at RA = 14<sup>h</sup>20<sup>m</sup>12<sup>s</sup>, Dec = 53°00′ with radius of 6′.0 has been selected for further processing. The exposure map of the individual observation resulting from various instrumental characteristics<sup>4</sup>, has a complex structure. In effect, the exposure map of the merged observation is even less regular and is devoid of any clear symmetries. On the other hand, a rough texture of the individual exposure is reduced and smoothed in a sum of 16 components. To reduce further the variations of the exposure map over the investigated area, a threshold of the minimum exposure has been set separately for both energy band. Pixels below this threshold have not been used in the calculations.

A threshold has been defined at ~ 75 % of the maximum value of the exposure map for the both energy bands. In effect, the maximum deviations of the exposure from the average value do not exceed 15 % and 18 % in the bands S and H, respectively, and the corresponding rms of the exposures amount to 5.9 and 6.2 %. In Table 2 the conversion factors calculated using the relevant amplitudes of the exposure maps are given. In the calculations “from counts to flux” a power spectrum with a photon index  $\Gamma_{\text{ph}} = 1.4$  was assumed (Kim et al., 2007).

Variations of the conversion factor,  $cf$ , over the investigated area alter the source fluxes via Eq. 6 and, consequently, the source counts  $N(S)$ . For the power law counts the  $cf$  uncertainty affects the counts normalization and does not change the slope. It is shown in the Appendix that – as long as the  $cf$  variations remain small – they modify the probability distributions  $P(r|1)$  and  $P(r)$  in such a way that the solution of Eq. 11 is not affected.

#### 3.2. The Point Spread Function

The *Chandra* X-ray telescope PSF is a complex function of source position and energy (e.g. Allen et al., 2004). However, to compute the nearest neighbor probability distribution for counts generated by a point-like source,  $\mathcal{P}(r|k)$ , we do not need a full

<sup>4</sup> To name the most obvious: vignetting, gaps between chips, telescope wobbling and all kinds of chip imperfections.

**Table 2.** Energy bands and conversion factors

Energy band [keV]	Average	Conversion factors <sup>a</sup>		
		rms	minimum	maximum
S 0.5 – 2	1.469	0.087	1.279	1.687
H 2 – 8	5.546	0.346	4.862	6.511

<sup>a</sup> The conversion factor (cf) has units of  $10^{-17}$  (erg·cm<sup>-2</sup>·s<sup>-1</sup>)/count.

model of the PSF shape. The aim is to find a convenient analytic PSF approximation adequately reproducing the NNST over the investigated area for each energy band. The model should be applicable to the merged AEGIS observations processed in a standard way.

To effectively compute the  $\mathcal{P}(r|k)$  we first construct a model PSF. Then, the relevant probability distributions are obtained using the Monte Carlo method. We note that the analytic form of the PSF should mimic the radial distribution of counts, while some deviations from the azimuthal symmetry are of lesser importance. Several simple analytic models have been tested to fit the observed distribution of counts and it was found that a function of the form

$$f(< r) = \frac{r^\alpha}{z + r^\alpha + y \cdot r^{\alpha/2}} \quad (12)$$

adequately represents the encircled count fraction (ECF), where  $\alpha$ ,  $z$ , and  $y$  are parameters depending on the source position and energy. Fits of Eq. 12 to the observed count distribution for several brightest sources have allowed us to find simple relationships between these parameters and the off-axis angle. The whole procedure looks as follows. We have noticed that the PSF parameters  $\alpha$ ,  $y$ , and  $\log z$  are satisfactorily approximated by linear functions of the off-axis angle  $\theta$ :

$$\alpha = a_\alpha \cdot \theta + b_\alpha \quad y = a_y \cdot \theta + b_y \quad \log z = a_z \cdot \theta + b_z, \quad (13)$$

where  $a_s$  and  $b_s$  ( $s = \alpha, y, z$ ) are six parameters which are substituted in Eq. 12 and simultaneously fitted to the observed distribution of counts in a number (25 and 31 in the S and H band, respectively) of the strongest point-like sources. In Fig. 1 a sample of the resultant fits to the observed distributions in the S band is shown. Since not all the fits are of equal quality, the effects of the  $\mathcal{P}(r|k)$  approximation are carefully examined. As a good envelope of errors generated by the imperfections of our fitting procedures we have constructed two model  $\mathcal{P}(r|k)$  distributions using the ECF functions systematically wider and narrower by 15% as compared to the best fit.

Example results of this procedure are illustrated in Fig. 2, where the envelope ECFs for two sources at 3'2 and 6'1 off axis angle are shown. Although some deviations are quite large, the observed ECFs are predominantly contained within the  $\pm 15\%$  distribution in a wide range of the separations  $r$ .

In the observational material used in the present investigation the maximum separations found in the NNST very rarely exceed 2". Thus, our fits appear adequate for the NNST and it is assumed that the  $\pm 15\%$  limits (indicated by the dotted curves in Fig. 2) define the maximum systematic errors associated with the PSF fitting procedure and will be used to assess uncertainties in our faint source calculations.

In the Monte Carlo computations of  $\mathcal{P}(r|k)$  a population of  $10^8$  "sources" of  $k = 2, 3, \dots, k_{\max}$  counts were distributed randomly over the investigated area<sup>5</sup>. The distribution of counts

<sup>5</sup> The value of  $k_{\max}$  is related to the sensitivity threshold and is different for each energy band; see below.

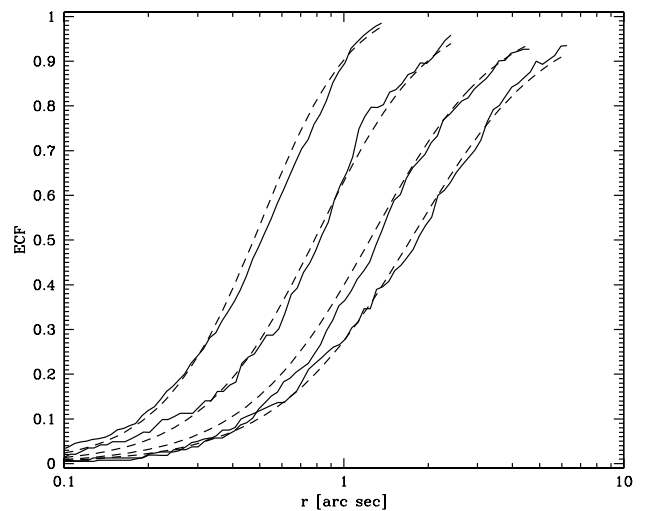


**Fig. 1.** Encircled count fraction (ECF) as a function of distance from the count centroid. Example distributions are shown for 4 sources at 1'0, 3'2, 5'0, and 6'1 from the field center. Solid curves – observed count distributions, dashed curves – fits obtained using Eqs. 12 and 13.

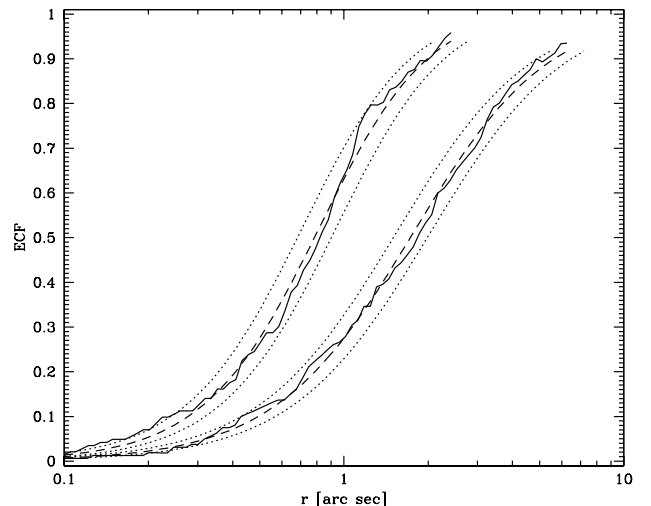


**Fig. 2.** ECF as in Fig. 1 for sources at 3'2 and 6'1 from the field center. Solid curves – observed count distributions, dashed curves – best fits obtained using Eqs. 12 and 13, dotted curves – the ECF distributions with the radius  $r$  scaled by  $\pm 15\%$ .

within each source was randomized according to the model ECF. Then, for each source a distribution of the nearest neighbor separations was determined and used to obtain the corresponding amplitudes of  $\mathcal{P}(r|k)$ . The procedure has been executed for the best fit and  $\pm 15\%$  ECF distributions.

### 3.3. The "afterglow" correction

A charge deposited by a cosmic-ray in the ACIS CCD detector may be released in two or more time frames generating a sequence of events, so-called "afterglow". The events span typically several seconds and do not need to occur in consecutive frames<sup>6</sup>. As a result, the data contain clumps of counts, which

<sup>6</sup> See <http://cxc.harvard.edu/ciao/why/afterglow.html> for details.

mimic very weak sources. Fortunately, the time sequences of such afterglow counts span short time intervals as compared to exposure times of all the observations. This allows us to unambiguously identify practically all the afterglows and remove them from the observation.

### 3.4. Pixel randomization

Positions of counts in the standard ACIS processing are randomized within the instrument pixel approximated by a square  $0'.492$  a side. Since the typical nearest neighbor separations are comparable to the pixel size, the NNST at small angular scales is smoothed by the count randomization. The effect is significant and generates most of the statistical noise in our calculations. To assess uncertainties introduced by the count randomization, 12 sets of randomized observations were produced using the original event data with non-randomized (integer) counts positions. Then, the NNST was determined for each observation and the data were used to obtain the slope  $b$  of the source number counts by means of Eq. 11. A scatter between the 12 count slope estimates represents the statistical error of the present method.

### 3.5. Strong source removal

To maximize effect of the weak source population on the NNST, the strong sources should be removed from the data. The threshold source flux is defined by  $k_{\max}$  counts in the Eq. 11. Thus, the value of  $k_{\max}$  should be set at a level sufficiently large to ensure that all the sources producing more counts than  $k_{\max}$  are found using standard source search criteria. On the other hand,  $k_{\max}$  should be small enough to warrant that the number of sources is adequately represented by the function  $N(s)$ .

A catalog of point sources in the AEGIS field is given by Laird et al. (2009). For each source listed in that paper, a radius  $r_{85}$  enclosing 85 % of counts has been calculated using the PSF at the source position. Then, several trial values of  $k_{\max}$  were applied to assess completeness threshold in the investigated area. It was found that for  $k_{\max} = 20$  all the brighter sources are clearly recognized, while this value is low enough to allow for statistical treatment of the population of still weaker sources.

## 4. The source counts

### 4.1. The soft band

Using the selection criteria given in Sect. 3, the area of the field and the total number of counts in the soft band amount to 97.5 sq. arcmin and 73711, respectively. After the removal of strong sources according to the procedure described above, the area is reduced to 92.7 sq. arcmin and the number of counts to 48737. The average count density amounts to 0.146 per sq. arcsec. and the average distance to the nearest neighbor for the random distribution is equal to  $1'.22$ . To eliminate a contamination of the count distribution by strong source photons in the PSF wings, the removal radius of  $\sim 4 \cdot r_{85}$  was applied.

The calculations have been performed as follows. First, the count distributions were used to calculate the  $P(r)$  and  $P(r|1)$  probabilities. The distribution of a distances to the nearest neighbor for each count defines the  $P(r)$ , while the distribution of the distances between the randomly distributed points and the nearest observed count is used to determine  $P(r|1)$ . The NNST has been formulated in the Sect. 2 using the cumulative probabilities, and estimates of the count slope  $b$  obtained from Eq. 11 for

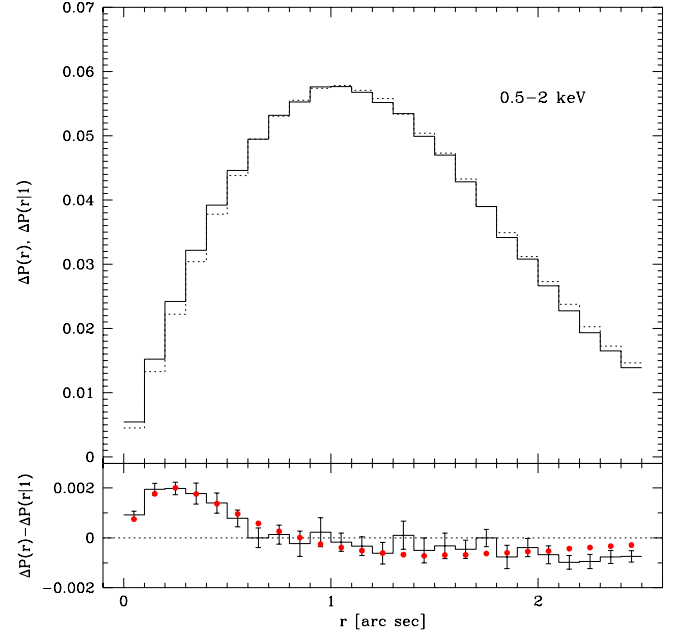


**Fig. 3.** The nearest neighbor probability distributions binned with  $\Delta r = 0'.1$  for the observed counts (solid histogram), and between random and observed counts (dotted histogram); error bars in the lower panel show  $1\sigma$  uncertainties.

different separations  $r$  are dependent. To obtain a set of independent equations, we use the differential probability distributions  $\Delta P(r) = P(r) - P(r + \Delta r)$ . In the calculations the relevant probability distributions have been obtained over the whole range of the observed separations with  $\Delta r = 0'.1$ . Then, using the Least Square method the best fit value of the count slope  $b$  has been determined for each of the randomized distributions. Finally, the average and rms of  $b$  was calculated. The rms obtained in this way results only from the randomization of counts.

To facilitate comparison of the present results with those available in the literature, we have adopted from Georgakakis et al. (2008) the number counts model for the bright sources. In effect, we fixed the normalization and the number counts slope in the flux range not covered by the present analysis, i.e. at fluxes above  $S = 2.9 \cdot 10^{-16}$  cgs or  $k_{\max} = 20$ . The present calculations provide the slope best estimate below that flux down to the level determined by the sources generating 2 counts. The average flux of those sources depends on the number counts slope and within the power law approximation amounts to  $S_w \approx (2 - b) \cdot cf$ , where  $cf = 1.469 \cdot 10^{-17}$  cgs is the average conversion factor (see Table 2).

The probability distributions  $\Delta P(r)$  and  $\Delta P(r|1)$  averaged over 12 data sets are presented in the upper panel of Fig. 3. A histogram in the lower panel shows the difference between the both distributions; the error bars indicate the histogram rms uncertainties obtained from the 12 pixel randomization. Dots show the model histogram obtained for the NNST best solution slope of  $b = 1.595$ .

In Fig. 4 the results based on the NNST for the S band are superimposed on the differential number counts presented by Georgakakis et al. (2008). The counts are normalized to the Euclidean slope of  $-2.5$ . Full dots and dotted line denote the counts and model by Georgakakis et al. (2008), open circles – the counts by Kim et al. (2007), and the dot-dash curve – the predicted AGN counts from Ueda et al. (2003). The thick line

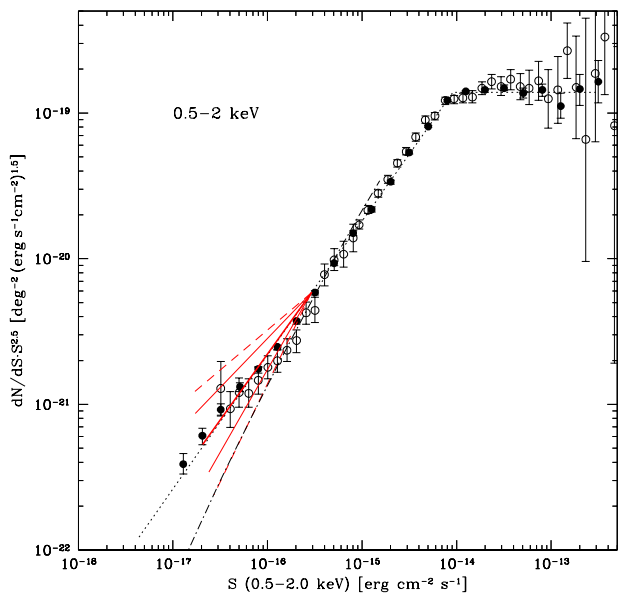


**Fig. 4.** Differential number counts in the 0.5 – 2 keV band normalized to the Euclidean slope. The data points and the dotted line are taken from Georgakakis et al. (2008); dot-dash curve shows the AGN model by Ueda et al. (2003); solid lines - the number counts estimates based on the NNST: thick solid line - the best power-law fit, thin solid lines -  $1\sigma$  uncertainty range due to the counting statistics; dashed lines - maximum total uncertainty including potential errors generated by inaccuracies of the PSF fitting. The count normalization at the bright end of the NNST model is fixed at the amplitude given by Georgakakis et al. (2008) approximation.

shows the NNST best fit solution with the slope  $b = 1.595$  and the normalization fixed at  $S = 2.9 \cdot 10^{-16}$  cgs. The number counts above that flux are described by the Georgakakis et al. (2008) model, i.e. over a wide range of fluxes the counts are approximated by the power law with the differential slope of  $-1.58$ . It is clear that the NNST solution is in full agreement with the direct source counts derived from the deep *Chandra* exposures. One should emphasize that the present NNST solution is based on the relatively shallow exposure as compared to the Georgakakis et al. (2008) data. In fact, the sources at the low flux end of the present solution on the average generate in our data essentially less than 2 counts each. Evidently, the NNST is capable to provide a sensitive estimation method for the population of sources which cannot be recognized as individual entities. It is worth to note that counts due to the sources generating the signal, i.e. producing  $2 \leq k \leq 20$  photons, constitute a small fraction of all the counts. In the present model just  $\sim 1080$  counts or 2.2% comes from these sources while the remaining 97.8% is distributed randomly.

#### 4.2. Error estimates

A small fractional contribution of counts produced by sources to the total number is to be blamed for the rather large statistical uncertainties of the NNST method. In our case the rms of the slope  $b$  in the S band amounts to 0.230. The situation is even worse in the H band, where the rms uncertainty of the slope reaches 0.34 (see below).

A question of systematic errors is less straightforward. Several potential effects could influence our estimate of the count slope. The first one, already discussed in Sect. 3.2, is associated with our PSF approximation. The complex shape and intricate position dependence of the PSF demands approximate treatment. Our PSF fits inevitably introduce errors. Unfortunately, an amplitude of these errors is difficult to assess. Because of that we adopted a cautious approach to this problem. Alongside the best fit PSF model we have considered two ancillary sets of PSFs which delineate the observed count distribution of the observed strong sources and also confine possible deviations introduced by our simplified model of the PSF variations over the field of view. Visual comparison of the actual count distributions and our model PSF shows that the  $\pm 15\%$  modification of the PSF width account for any potential deficiencies of our PSF calculations.

The  $\pm 15\%$  uncertainty of the PSF width introduces a substantial uncertainty of the slope estimate. For the PSF wider than the best fit by 15% we get  $b = 1.744 \pm 0.207$ , while for the 15% narrower,  $b = 1.421 \pm 0.267$ . One can summarize these results as follows. Statistical  $1\sigma$  limits around the best fit solution of  $b = 1.595$  are defined as  $1.365 < b < 1.825$ , while the combined statistical and systematic uncertainties are  $1.154 < b < 1.951$ . The statistical uncertainties are shown in Fig. 4 with thin solid lines and the total uncertainties – with dashed lines. One should note that these “total” error estimates are highly conservative. They have been obtained by simple addition of the systematic and statistical errors assuming their highest “possible” values.

Another source of the slope estimate error is related to the uncertainty of the number counts normalization. Any modification of the number of sources at the strong flux end affects the count slope as well. However, in the relevant flux range the realistic normalization uncertainties remain small (see Fig. 4) and do not affect considerably the slope uncertainty range.

Variations of the conversion factor over the field of view also do not play significant role in our slope estimates. As pointed out in Sect. 3.1, one can incorporate these variations within the investigated area into uncertainty of the count normalization  $N_o$ . Assuming the differential number counts  $N(S) = \mathcal{N}S^{-b}$  (with flux  $S$  in  $\text{erg cm}^{-2}\text{s}^{-1}$ ), a relationship between the count normalization  $N_o$  and the conversion factor  $cf$  is

$$N_o = \mathcal{N} \cdot cf^{1-b}. \quad (14)$$

Thus, for  $b = 1.595$  and the rms of the conversion factor at the level of  $\sim 5.9\%$  (Table 2), the uncertainty of  $N_o$  amounts to  $\sim 3.5\%$  and is small in comparison with the uncertainty of  $\mathcal{N}$  itself.

Substantial variations of the PSF width with the distance from the telescope axis limit the effectiveness of the NNST method. This is because the nearest neighbor distribution  $P(r)$  for the Eq. 11 is estimated using the actual data, i.e. actual distribution of sources, while the probability  $\mathcal{P}(r|k)$  is determined by averaging the model sources over the field of view. This feature introduces additional uncertainty if the number of sources generating  $k \approx k_{\text{max}}$  is small, but should be of lesser importance in the deep *Chandra* exposures.

#### 4.3. The hard band

A fraction of counts produced by discrete sources to all the counts in the 2 – 8 keV band is substantially smaller than in the 0.5 – 2 keV band. In effect, the NNST method is less effective in the H than in the S band, i.e. the slope estimates in the H band are subject to higher statistical uncertainties. Here we briefly summarize the results in the H band.

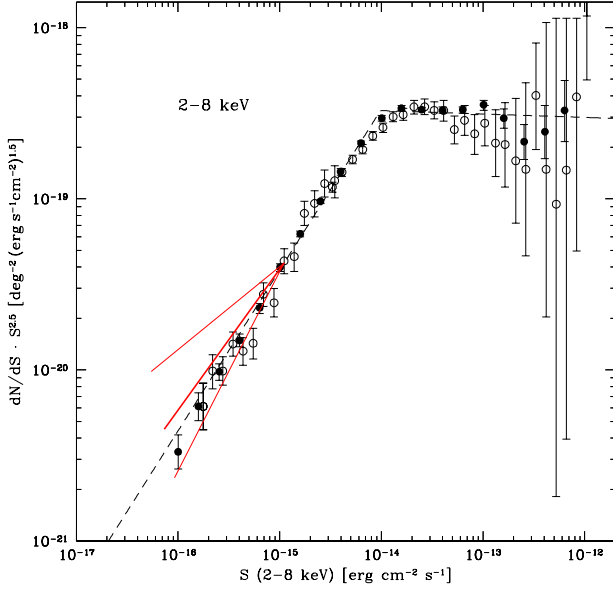


**Fig. 5.** Differential number counts in the 2 – 8 keV band normalized to the Euclidean slope. The data points and the dashed line are constructed using the 2 – 10 keV band from Georgakakis et al. (2008); solid lines - the number counts estimates based on the NNST: thick solid line - the best power-law fit, thin solid lines -  $1\sigma$  uncertainty range due to the counting statistics.

As a reference data we used those published by Georgakakis et al. (2008). The counts and the analytic fit in the band 2 – 10 keV given in that paper were converted to the band 2 – 8 keV assuming a power spectrum with the photon index  $\Gamma = -1.4$ .

After the removal of strong sources, the area and the number of counts used in the NNST amount to 94.4 sq. arcmin and 101596, respectively. Applying the same procedure as in the S band, the best fit slope  $b = 1.676 \pm 0.340$  was found using the 12 randomized distributions. This is shown in Fig. 5 with a thick line and two thin lines. The sources represented by the NNST solution, i.e. sources producing  $2 \leq k \leq 20$  counts, contribute just  $1214^{+979}_{-427}$  photons or  $1.19^{+0.96}_{-0.42}$  % of all the counts. Due to large statistical uncertainty in this band the NNST does not provide tight limits on the number counts and we have not plotted here lines representing the range of systematic uncertainties.

## 5. Conclusions

We have estimated the source number counts in the S band down to  $\sim 2 \cdot 10^{-17}$  cgs using the merged data with the integrated exposure time of  $\sim 465$  ks. This flux level is below the standard detection threshold for individual sources in the deepest *Chandra* exposures of 2 Ms (Kim et al., 2007).

Our slope estimate below  $S = 10^{-16}$  cgs fits perfectly the actual discrete source counts determined using such deep observations. It shows the NNST potential as an effective tool in the investigation of the extremely weak source population. In the second paper of this series we plan to apply the NNST method to the *Chandra* Deep Fields. With a 2 Ms exposure the NNST will allow to assess number counts down to  $\sim 4 \cdot 10^{-18}$  cgs in the 0.5 – 2 keV band and to  $\sim 2 \cdot 10^{-17}$  cgs in the 2 – 8 keV band,

although in the latter case the expected accuracy of our estimate might be quite low.

The constraints obtained for the H band are not restrictive. This is because the contribution of the non X-ray counts increases with energy and the data become strongly contaminated by the particle background which effectively “dilutes” the counts concentrations produced by the sources. In the next paper some prospects to improve the S/N ratio above 2 keV will be explored.

*Acknowledgements.* I thank all the people generating the Chandra Interactive Analysis of Observations software for making a really user-friendly environment. This work has been partially supported by the Polish KBN grant 1 P03D 003 27.

## References

- Allen, C., Jerius, D. H., & Gaetz, T. J. 2004, Proc. SPIE, 5165, 423  
 Galeazzi, M., Gupta, A., Covey, K., & Ursino, E. 2007, ApJ, 658, 1081  
 Georgakakis, A., Nandra, K., Laird, E. S., Aird, J., & Trichas, M. 2008, MNRAS, 388, 1205  
 Hasinger, G. 1992, in X-ray Emission from Active Galactic Nuclei and the Cosmic X-ray Background, ed. Brinkmann & Trümper, MPE Report no. 235, 321  
 Hasinger, G., Burg, R., Giacconi, R., et al. 1993, A&A, 275, 1  
 Henley, D. B., Shelton, R. L., & Kuntz, K. D. 2007, ApJ, 661, 304  
 Kim, M., Wilkes, B. J., Kim, D.-W., et al. 2007, ApJ, 659, 29  
 Laird, E. S., Nandra, A., Georgakakis, A., et al. 2009, ApJS, 180, 102  
 Lehmann, I., Hasinger, G., Schmidt, M., et al. 2001, A&A, 371, 833  
 Miyaji, T., & Griffiths, R. E. 2002, ApJ, 564, L5  
 Sołtan, A. M. 1991, MNRAS, 250, 241  
 Sołtan, A. M. 2007, A&A, 475, 837  
 Sołtan, A. M. 2003, A&A, 408, 39  
 Ueda, Y., Akiyama, M., Ohta, K., & Miyaji, T. 2003, ApJ, 598, 886

## Appendix A: Impact of the exposure fluctuations on the NNST

Effects of the small variations of the exposure over the field of view on the probability distributions  $P(r)$  and  $P(r|1)$  in Eq. 11 are investigated.

The observed distribution of counts is considered here as the realization of a Poisson process. According to this premise, the probability of getting an event in the  $x - y$  plane of the field of view (fov) is described by a smooth function  $\rho(x, y)$ . The  $\rho(x, y)$  amplitude is proportional to the exposure map (Sect. 3.1). One can define the “true” probability density  $\rho_o(x, y)$  which would describe the distribution of counts expected for the perfect instrument with the flat exposure map and - consequently - a constant conversion factor. Thus, the  $\rho$  distribution is related to the  $\rho_o$  and the fluctuations of the exposure map, EM:

$$\rho(x, y) = \rho_o(x, y) \cdot \frac{\text{EM}(x, y)}{\text{EM}_o}, \quad (\text{A.1})$$

where  $\text{EM}_o$  is the exposure map of the perfect instrument. A natural normalization of the exposure map is assumed:  $\langle \text{EM}(x, y) \rangle = \text{EM}_o$ , where the brackets  $\langle \dots \rangle$  denote the averaging over the fov. Since the distributions  $\rho_o$  and EM are independent,  $\langle \rho \rangle = \langle \rho_o \rangle$ . To quantify the amplitude of the EM fluctuations with a single parameter  $\varepsilon$ , we define a function  $f(x, y)$ :

$$\varkappa(x, y) = \frac{\text{EM}(x, y)}{\text{EM}_o} = 1 + \varepsilon f(x, y), \quad (\text{A.2})$$

in such a way that  $\langle f \rangle = 0$  and  $\sigma_f^2 = \langle f^2 \rangle = 1$ . We also have  $\langle \varkappa \rangle = 1$  and  $\sigma_\varkappa = \varepsilon$ , where  $\sigma_\varkappa$  is the rms of  $\varkappa$ . Since  $\sigma_\varkappa = \sigma_{\text{EM}}/\text{EM}_o$ , the data in the Table 2 show the  $\varepsilon$  parameter

characterizing the present observational material remains small; in particular, it is equal to 0.059 and 0.062 for energy bands S and H, respectively.

The expected nearest neighbor probability distributions  $P(r|1)$  and  $P(r)$  are related to the count distribution  $\rho$  in a following way:

$$P(r|1) = \langle e^{-\pi r^2 \rho(x,y)} \rangle, \quad (\text{A.3})$$

$$P(r) = \frac{1}{\langle \rho \rangle} \langle \rho(x,y) \cdot e^{-\pi r^2 \rho(x,y)} \rangle. \quad (\text{A.4})$$

Substituting Eqs. A.1 and A.2 into Eqs. A.3 and A.4 one can expand the distributions  $P(r|1)$  and  $P(r)$  in powers of the parameter  $\varepsilon$ . Since the distributions of  $f(x,y)$  and  $\rho_o(x,y)$  are uncorrelated, one finds that the linear term in  $\varepsilon$  vanishes.